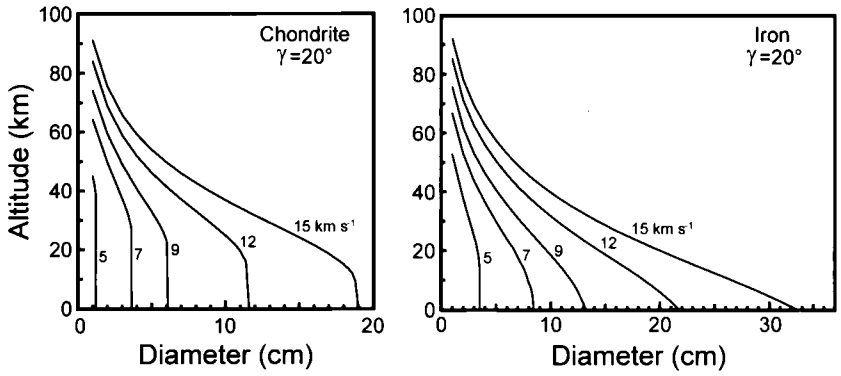

Fig. 4. Survival of chondritic and iron meteorites of various sizes that enter the martian atmosphere at a constant angle (20° from the horizontal) over a range of velocities from 5 to 15 km s^{-1}.

ported in any surface images; some 100 such craters per square kilometer are recorded even on the youngest surfaces of Mars (*5*). Although superposition by subsequent craters and their ejecta destroyed some of these craters, the relatively old Viking and Pathfinder sites should be pervasively cratered at scales of 10 m, yet none of this cratering record is obvious in the surface images. Our search included potential secondary craters associated with Big Crater (*14*) that should have produced ejecta impacting at some 100 m s^{-1} at the Pathfinder site. Such velocities suffice to make craters in unconsolidated fines, yet none is recognizable. Currently we have no explanation for the apparent lack of small craters in the Pathfinder and Viking images. Compared with the highly comminuted, fine-grained lunar regoliths, the Pathfinder and Viking surfaces appear to be dominated by coarse rubble. While investigating the comminution of fragmental targets whose size distribution was dominated by fragments larger than the projectile (*19*), we typically produce craters that are relatively shallow and have poorly developed rims. It seems possible that martian regolith craters are similarly shallow and that they are readily modified by aeolian infill beyond recognition. Aeolian processes, however, are not energetic enough to erode the impact record in competent rocks with comparable efficiency.

Quantitative ramifications of this emerging small-scale impact environment on Mars remain to be determined and depend on the absolute impactor flux (*5*). Nevertheless, consistent with (*5, 15*), the martian surface should be more dynamic than postulated by (*6, 8*). Relative to the moon, the roles of craters of >10 m will be similar on Mars, yet the effect of meter-sized events is greatly diminished, and craters smaller than a few centimeters will be absent on Mars.

References and Notes

1. H. Heiken *et al.*, Eds. *Lunar Sourcebook* (Cambridge Univ. Press, Cambridge, 1991).
2. R. P. Binzel *et al.*, Eds. *Asteroids II* (Univ. of Arizona Press, Tucson, 1989).
3. R. D. Dycus, *Publ. Astron. Soc. Pac.* **81**, 399 (1969).
4. D. E. Gault and R. S. Baldwin, *Eos* **51**, 343 (1970).
5. W. K. Hartmann, *Met. Planet. Sci.* **34**, 167 (1999).
6. M. P. Golombek *et al.*, *Science* **278**, 1743 (1997).
7. P. H. Smith *et al.*, *ibid.*, p. 1758.
8. M. P. Golombek *et al.*, *J. Geophys. Res.* **104**, 8523 (1999).
9. R. Greeley *et al.*, *ibid.*, p. 8573; N. T. Bridges *et al.*, *ibid.*, p. 8595.
10. F. Hörz *et al.*, *ibid.* **76**, 5770 (1971); D. E. Gault, *Moon* **4**, 32 (1973).
11. A. Fujiwara *et al.*, in *Asteroids II*, R. P. Binzel *et al.*, Eds. (Univ. of Arizona Press, Tucson, 1989), p. 240.
12. T. A. Mutch, *The Martian Landscape*, NASA SP 425 (1978); R. Arvidson *et al.*, *Rev. Geophys. Space Phys.* **27**, 39 (1989).
13. J. W. Rice *et al.*, *Lunar Planet. Sci.* **30**, abstr. 2063 (1999).
14. M. S. Stefanis and H. J. Moore, *ibid.*, abstr. 1409.
15. A. T. Basilevsky *et al.*, *J. Geophys. Res.* **104**, 8617 (1999).
16. W. C. Rochelle *et al.*, *Eighth Annual Thermal and Fluids Analysis Workshop*, NASA CP 3359 (1997). The calculations used the simulation and optimization of rocket trajectories (SORT) program, a trajectory code using drag coefficients of spheres in combination with the object-reentry survival analysis tool (ORSAT) subroutine, which treats aerothermal effects and ablation processes. Mars's northern-summer atmosphere [W. Hansen *et al.*, JPL Report at COSPAR, Innsbruck, Austria (1978), p. 113] was added to SORT, along with an aeroheating subroutine for CO_2 atmospheres. For additional details consult W. C. Rochelle *et al.*, *Lunar Planet. Sci.* **30**, abstr. 1651 (1999).
17. A. Vasavada *et al.*, *J. Geophys. Res.* **98**, 3469 (1993).
18. P. A. Bland and T. B. Smith, *Lunar Planet. Sci.* **30**, abstr. 1673 (1999).
19. F. Hörz and M. J. Cintala, *Met. Planet. Sci.* **32**, 179 (1997).
20. Discussions with R. V. Morris, A. T. Basilevsky, and M. Golombek were most helpful, as were the comments of two anonymous reviewers. We dedicate this paper to the memory of D. E. Gault, who pioneered the experimental study of planetary impacts.

1 June 1999; accepted 3 August 1999

Defect-Mediated Condensation of a Charge Density Wave

Hanno H. Weitering,[1,2] Joseph M. Carpinelli,[1,2] Anatoli V. Melechko,[1,2] Jiandi Zhang,[3] Miroslaw Bartkowiak,[1,2] E. Ward Plummer[1,2]

Symmetry, dimensionality, and disorder play a pivotal role in critical phenomena. The atomic imaging capabilities of the scanning tunneling microscope were used to directly visualize the interaction between charge density oscillations and lattice defects in a two-dimensional charge density wave (CDW) system. Point defects act as nucleation centers of the CDW, which, as the temperature is lowered, results in the formation of pinned CDW domains that are separated by atomically abrupt charge boundaries. Incomplete freezing of substitutional disorder at low temperature indicates a novel CDW-mediated hopping of pinning centers.

A charge density wave (CDW) is a broken symmetry state of a metal. It incorporates a periodic modulation of the crystal's valence charge and is usually accompanied by a small periodic lattice distortion (*1*). In simple terms, the symmetry-breaking charge modulation (which is not necessarily commensurate with the crystal lattice) lowers the energy of the occupied electron states and raises that of the unoccupied states, opening up a band gap, so that the CDW state could become stable below a certain critical temperature T_c. A classic example is the Peierls distortion in quasi–one-dimensional compounds such as $K_2Pt(CN)_4Br_{0.3}\cdot 3H_2O$ (known as Krogmann's salt) or transition metal bronzes such as $K_{0.3}MoO_3$ (*1*). The Peierls transition is a second-order phase transition. The thermodynamic order parameter that characterizes the broken symmetry phase can be related to the magnitude of the single-particle band gap or the amplitude of the lattice distortion, which both vanish above T_c. CDW transitions in quasi–two-dimensional compounds can be first order and are not necessarily accompanied by a metal-nonmetal transition (*2*).

Charged impurities can alter the phase and amplitude of the condensate near the impurity

[1]Department of Physics and Astronomy, University of Tennessee, Knoxville, TN 37996, USA. [2]Solid State Division, Oak Ridge National Laboratory, Oak Ridge, TN 37831, USA. [3]Department of Physics, Florida International University, University Park, Miami, FL 33199, USA.

site and may even prohibit long-range ordering (*1*). Theoretical studies with Ising models have indicated that crystalline order will be completely destroyed by the random external field (that is, impurities) if the system dimension $d \leq 2$ (*3, 4*). Even a first-order phase transition may be preempted by tiny amounts of randomly placed defects, despite the fact that correlation lengths remain finite near the critical point (*5–7*).

Experimentally, critical behavior is usually studied with momentum-space probes such as x-ray diffraction or neutron scattering or with measurements of macroscopic thermodynamic quantities such as heat capacity or susceptibility. None of these measurements provide direct information about the role of disorder. Scanning tunneling microscopy (STM) has been used to image the surfaces of bulk CDW materials, and although perturbations in the CDW amplitude have been attributed to subsurface defects, these defects could not be identified or imaged directly (*8*). We used STM to visualize the interaction between point defects and a CDW localized at a crystal surface to show how point defects locally perturb the static charge-ordering coherency, how CDW domains nucleate, what determines their registry and size, and how all of this ultimately affects the order parameter and critical behavior of the CDW condensate. An unexpected finding is that, for our particular CDW system, point defects do not act as a fixed random perturbation, as is the case in the well-known random-field model of statistical mechanics (*3, 4*). Rather, their spatial distribution is influenced by the nucleating density wave. In other words, point defects and collective CDW oscillations are interactive.

Our system of choice is the recently discovered CDW at the ultrathin Sn/Ge(111)-α interface (*9*, *10*). The interface consists of one-third of a monolayer of Sn atoms chemisorbed on a Ge(111) crystal surface, forming a $(\sqrt{3} \times \sqrt{3})R30°$ hexagonal arrangement, as shown in Fig. 1 (*11*). This ordered overlayer is produced by Sn deposition onto the clean Ge(111)-c(2 × 8) surface in ultrahigh vacuum, followed by a brief anneal at temperature $T \approx 500$ K. A pair of registry-aligned STM images (Fig. 2) acquired at low temperature ($T \approx 60$ K) shows the real-space distribution of the empty and filled electron states in the Sn overlayer. The insets in Fig. 2 show room temperature data. Each protrusion corresponds to the dangling bond of a Sn atom; substrate atoms cannot be seen in STM (*9*, *10*). At room temperature, all Sn atoms appear with equal intensity in STM, regardless of the tunneling polarity (insets in Fig. 2). At low temperature, however, a CDW superstructure is visible: One of three Sn atoms has an enhanced electron density in its dangling bond orbital, apparently at the expense of the other two. The empty-state image highlights atoms that are depleted of charge and form a bright honeycomb sublattice. The filled-state image highlights atoms that acquire charge and form a bright hexagonal sublattice. The CDW superperiod is (3 × 3) with respect to the underlying Ge(111) lattice. Because there are three atomic sites within the (3 × 3) supercell, there are three possible domain orientations on the surface. Figure 3A shows a filled-state STM image with seven domain patches. Figure 3B displays the same image but with a colored overlay grid that identifies the three possible domains (yellow, red, and blue).

Defects have a crucial role in defining the CDW domain structure on the surface. There are two main kinds of defects usually found in this overlayer structure: vacancies (<1% of atom sites) and substitutional impurities (2 to 5% of atom sites). Vacancies (not shown) appear "black" at both tunneling polarities. Substitutional impurities can only be seen in the empty-state image, indicating that they are depleted of charge. They are in fact Ge atoms that occupy Sn sites (*12, 13*). All five lattice defects in Fig. 2 are substitutional Ge atoms. Within a single CDW domain, substitutional Ge atoms are positioned on the bright honeycomb sublattice of the empty-state image (Fig. 2A). The filled-state STM image in Fig. 2B also illustrates this point: None of the five Ge substitutional defects coincide with a charge density maximum. If one of the other two domain types

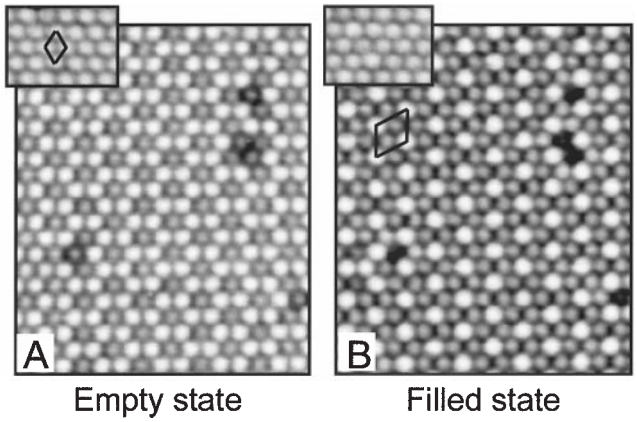

Fig. 2. Registry aligned (**A**) empty-state and (**B**) filled-state STM images of the Sn overlayer at low temperature. Insets show STM images of the Sn layer at room temperature. The $(\sqrt{3} \times \sqrt{3})R30°$ and (3 × 3) unit cells are indicated. The complementary filled-state and empty-state images at low temperature indicate the existence of a commensurate in-plane charge ordering. The (3 × 3) CDW phase is a $(\sqrt{3} \times \sqrt{3})R30°$ superstructure of the room temperature phase, which in turn is a $(\sqrt{3} \times \sqrt{3})R30°$ superstructure of the ideal Ge(111)-(1 × 1) lattice underneath. All overlayer lattice sites that appear black in the filled state image contain a substitutional Ge atom impurity. (bias voltage $V_{sample} = \pm 1.0$ V).

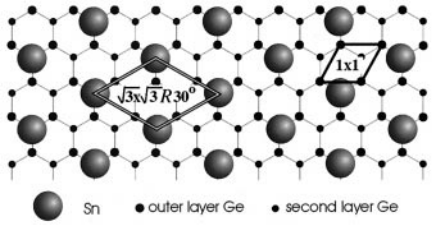

Fig. 1. Ball model of the α phase of Sn/Ge(111); Sn coverage is one-third of a monolayer. The indicated unit cell is a $(\sqrt{3} \times \sqrt{3})R30°$ supercell of the bulk truncated Ge(111)-(1 × 1) unit cell.

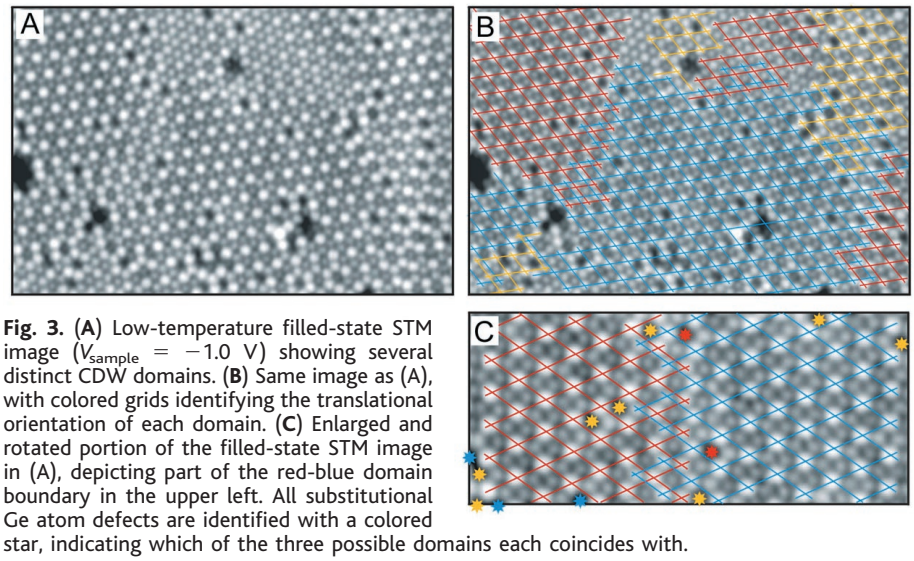

Fig. 3. (**A**) Low-temperature filled-state STM image ($V_{sample} = -1.0$ V) showing several distinct CDW domains. (**B**) Same image as (A), with colored grids identifying the translational orientation of each domain. (**C**) Enlarged and rotated portion of the filled-state STM image in (A), depicting part of the red-blue domain boundary in the upper left. All substitutional Ge atom defects are identified with a colored star, indicating which of the three possible domains each coincides with.

would have formed in this region, then either two or three of the substitutional defects would have coincided with a charge density maximum and forced a partial filling of the Ge dangling bond, which, evidently, is energetically unfavorable (*13*). These observations make clear that the type of CDW domain (yellow, red, or blue in Fig. 3) is fully determined by the registry of substitutional defects within that same area.

The domain morphology of the surface CDW can now also be understood. Figure 3C shows an enlarged and rotated section of the image in Fig. 3B, displaying part of the upper left, red-blue boundary. At this atomically abrupt domain boundary, each CDW domain dies off as it enters a region where the defect arrangement will not support its existence. The defects in Fig. 3C are labeled with colored stars, each identified with the domain type that it locally disallows. The numerous yellow defects would make it nearly impossible for any kind of long-range, yellow charge-ordered domain type to form in this portion of the sample. The red defects, as well as a few blue ones out of the field of view for Fig. 3C, define the position of the domain boundary. At the intersection of all three different possible domain types, a patch of apparently CDW-free area results, as can be identified in a few distinct patches at the top of Fig. 3A. These quenched regions must be the undistorted $(\sqrt{3} \times \sqrt{3})R30°$ phase, stabilized by the particular arrangement of the substitutional defects.

The low-temperature STM observations provide simple empirical rules that explain the static configuration of the CDW domains and their boundaries. Room-temperature images near point defects, however, provide important insights on the formation mechanism of the CDW condensate. A vacancy defect and a substitutional defect are shown in Fig. 4, A and B, respectively. These images, obtained at room temperature, reveal that both types of defects induce a strongly damped, local perturbation of the charge. The local charge ordering near the vacancy is similar to that of the CDW phase, that is, a (3×3) hexagonal superlattice in the filled-state image (Fig. 4A) and a bright honeycomb pattern in the empty-state image (not shown). The charge perturbation surrounding an isolated Ge substitutional defect is complementary to that of vacancy defects (and that of the CDW phase); that is, the filled-state image shows the honeycomb pattern with the Ge atom again positioned at the charge minimum, appearing as a dark spot (Fig. 4B).

The low-temperature images have shown that the arrangements of the CDW domains and domain boundaries are determined by the distribution of substitutional defects. However, the near-perfect arrangement of the Ge defects on CDW minima at low temperature also indicates that their distribution is not at all random; there appears to be a short-range correlation on a length scale comparable to the domain size. A detailed statistical analysis of defect distributions as a function of temperature will be presented elsewhere (*14*). Here, we provide a simple argument as to why the defect distribution in the low-temperature phase cannot be random, as one would normally expect. Statistically, the probability $P(m)$ of finding m out of n Ge defects at "wrong" lattice sites (that is, CDW maxima) on a domain of N lattice sites is given by

$$P(m) = \left[\frac{n!(N-n)!}{N!}\right] \times \left[\frac{\left(\frac{2}{3}N\right)!}{(n-m)!\left(\frac{2}{3}N-n+m\right)!}\right] \times \left[\frac{\left(\frac{1}{3}N\right)!}{m!\left(\frac{1}{3}N-m\right)!}\right]$$

We counted the number of "right" $(n - m)$ and "wrong" (m) defects on a collection of 16 CDW domains with well over 100 lattice sites and found that the number of wrong defects is well outside the standard deviation of this hypergeometric distribution. For instance, on a $N = 378$ domain, there are 11 substitutional defects, and only 1 is located at a CDW maximum, which indicates that the Ge defects are not randomly distributed in the CDW phase. At room temperature, however, defects are always distributed randomly (*14*), implying that the Ge substitutional defects can make at least a single hop when the CDW transition sets in. This (limited) atomic motion at or below room temperature appears reversible. Evidently, the CDW provides a mechanism that lowers the energy barrier for single-atom hops. Once the defects are in place, the CDW domains are firmly pinned. Motion of pinning sites in response to the formation of a CDW has been thought to account for the anomalous electrical transport properties of bulk $Rb_{0.30}MoO_3$ below the Peierls transition (*15*), although direct evidence is still lacking.

The nonrandomness of the defect distribution in the CDW phase cannot be concluded from a casual inspection of selected (3×3) domains. We therefore verified the existence of short-range defect correlations by simulating the nucleation of CDW domains on a computer using a Voronoi (or extended Wigner-Seitz) model of grain growth from randomly distributed nucleation seeds (point defects) (*16*). On the basis of computer simulations of 6000 Voronoi structures of various sizes corresponding to typical STM images, we conclude that the statistical distribution of the number of defects within the coalesced simulated CDW domains is inconsistent with the STM observations, indicating that the experimentally observed defect distribution at low temperature is in fact nonrandom.

The presence of local CDW patches nucleated at point defects at room temperature and patches of an undistorted $(\sqrt{3} \times \sqrt{3})R30°$ arrangement in regions of destructive interference (Fig. 3A) well below the previously reported T_c of 210 K (*10*) implies that the phase transition cannot be sharp. Variable temperature imaging indicates that local (3×3) patches near defects observed at room temperature spread out when the temperature is lowered (*14*). Even at $T = 130$ K, one can still associate the domains with individual point defects; that is, defect-driven spatial fluctuations still persist, and the long-range order parameter vanishes in the limit of infinite system size (*14*). Figure 4C shows the temperature dependence of the (3×3) beams in low-energy electron diffraction (LEED). The CDW transition is very gradual and does not exhibit universal behavior; diffraction data do not indicate a critical point.

On the basis of first-principles molecular dynamics simulations, Avila *et al.* (*17*) concluded that the CDW transition of Sn on Ge(111) is an order-disorder rather than a displacive phase transition as originally proposed (*9, 10*), similar to the well-known $(2 \times 1) \rightarrow c(4 \times 2)$ ordering transition of buckled

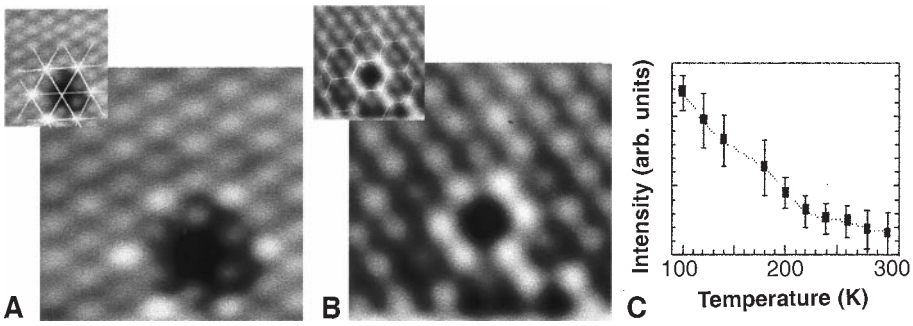

Fig. 4. Filled-state STM images ($V_{sample} = -1.0$ V) showing the local charge perturbations near two different point defects. (**A**) Charge rearrangement near a single-vacancy defect. Bright atoms are located on the (3×3) hexagonal grid shown in the inset. (**B**) Charge rearrangement near a substitutional Ge defect. Bright atoms are located on the corners of the honeycomb grid shown in the inset. Dim atoms are located at the center of the honeycombs. (**C**) Temperature dependence of the (1/3, 1/3) beam in LEED.

Si dimers on Si(100) (*18*). Inoue *et al.* have mapped the Si(100) surface onto a two-dimensional Ising Hamiltonian in a random magnetic field (to simulate defect pinning) and performed Monte Carlo simulations to model its thermodynamic behavior (*19*). They showed that the anticipated second-order phase transition in Si(100) is smeared out by defects. Our observations are consistent with their analysis. A difference from the Si(100) scenario is that the triangular Sn/Ge(111) system with static disorder should be mapped onto the random-field three-state Potts model rather than onto an Ising model (*20*). Most importantly, however, the substitutional disorder in these triangular lattice systems is neither static nor completely random, as is the case in the random-field model of statistical physics. Because the effects of quenched randomness are especially profound when $d \leq 2$, it would be interesting to explore when and how the defect degrees of freedom alter the conclusions of the random-field model.

References and Notes

1. G. Grüner, *Density Waves in Solids* (Addison-Wesley, Reading, MA, ed. 1, 1994).
2. J. A. Wilson, F. J. DiSalvo, S. Mahajan, *Adv. Phys.* **24**, 117 (1975).
3. Y. Imry and S.-K. Ma, *Phys. Rev. Lett.* **35**, 1399 (1975).
4. D. S. Fisher, G. M. Grinstein, A. Khurana, *Phys. Today* **41**, 56 (December 1988).
5. M. Aizenman and J. Wehr, *Phys. Rev. Lett.* **62**, 2503 (1989).
6. K. Hui and A. N. Berker, *ibid.*, p. 2507.
7. J. Cardy, *Physica A* **263**, 215 (1999).
8. X. L. Wu and C. M. Lieber, *Phys. Rev. B* **41**, 1239 (1990); B. Giambattista, C. G. Slough, W. W. McNairy, R. V. Coleman, *ibid.*, p. 10082.
9. J. M. Carpinelli, H. H. Weitering, R. Stumpf, E. W. Plummer, *Nature* **381**, 398 (1996).
10. J. M. Carpinelli, H. H. Weitering, M. Bartkowiak, R. Stumpf, E. W. Plummer, *Phys. Rev. Lett.* **79**, 2859 (1997).
11. J. J. Metois and G. Le Lay, *Surf. Sci.* **133**, 422 (1983).
12. J. M. Carpinelli, H. H. Weitering, E. W. Plummer, *ibid.* **401**, L457 (1998).
13. R. Stumpf, J. M. Carpinelli, H. H. Weitering, *Phys. Rev. B* **59**, 15779 (1999).
14. A. V. Melechko, J. Braun, H. H. Weitering, E. W. Plummer, in preparation.
15. J. Dumas, A. Arbaoui, H. Guyot, J. Marcus, C. Schlenker, *Phys. Rev. B* **30**, 2249 (1984).
16. D. Weaire and N. Rivier, *Contemp. Phys.* **25**, 59 (1984); M. Bartkowiak, unpublished material.
17. J. Avila *et al.*, *Phys. Rev. Lett.* **82**, 442 (1999).
18. P. C. Weakliem, G. W. Smith, E. A. Carter, *Surf. Sci.* **232**, L219 (1990).
19. K. Inoue, Y. Morikawa, K. Terakura, M. Nakayama, *Phys. Rev. B* **49**, 14774 (1994).
20. S. Alexander, *Phys. Lett. A* **54**, 353 (1975); M. Schick, J. S. Walter, M. Wortis, *Phys. Rev. B* **16**, 2205 (1977). A possible first-order transition would also be preempted by random defects as discussed in (*5*–*7*).

21. We thank T. Einstein, T. Lubensky, and K. Terakura for enlightening discussions. This work was supported by the NSF under grants NSF-DMR 9705246 (H.H.W.) and NSF-DMR 9801830 (E.W.P.). Oak Ridge National Laboratory is managed by Lockheed Martin Energy Research Corporation for the U.S. Department of Energy under contract DE-AC05-96OR22464.

9 June 1999; accepted 11 August 1999

Evidence for Quantum Critical Behavior in the Optimally Doped Cuprate $Bi_2Sr_2CaCu_2O_{8+\delta}$

T. Valla,[1] A. V. Fedorov,[1] P. D. Johnson,[1] B. O. Wells,[1,4] S. L. Hulbert,[2] Q. Li,[3] G. D. Gu,[5] N. Koshizuka[6]

The photoemission line shapes of the optimally doped cuprate $Bi_2Sr_2CaCu_2O_{8+\delta}$ were studied in the direction of a node in the superconducting order parameter by means of very high resolution photoemission spectroscopy. The peak width or inverse lifetime of the excitation displays a linear temperature dependence, independent of binding energy, for small energies, and a linear energy dependence, independent of temperature, for large binding energies. This behavior is unaffected by the superconducting transition, which is an indication that the nodal states play no role in the superconductivity. Temperature-dependent scaling suggests that the system displays quantum critical behavior.

Understanding transport in the cuprate superconductors and other synthetic metals is at the heart of current research in solid-state physics. There is speculation that the elementary excitations in these materials might well be drastically different from those in traditional metals where Fermi liquid theory has proved most successful (*1*). Angle-resolved photoemission (ARPES) has been an important experimental probe of the electronic excitations, providing insight into the fundamental interactions and quantities, such as the single-particle self energy Σ. The self energy reflects the interaction of the excitation with its local environment: the real part describing the screening of the excitation and the imaginary part describing the inverse lifetime. These microscopic properties are reflected in macroscopic behavior such as conductivity and the optical response. In two-dimensional (2D) systems, the self-energy effects measured in photoemission reflect solely the response to the photohole created in the emission process. As such, ARPES has provided a number of important insights into the cuprates, where the superconductivity is believed to be associated with the 2D CuO_2 planes. Highlights from ARPES include mapping of the Fermi surface (*2*), the identification of d-wave symmetry of the order parameter in the superconducting state (*3*), and the detection of a pseudogap for underdoped compounds above the transition temperature T_c (*4, 5*). However, the limited energy and momentum resolution of ARPES to date have meant that a quantitative determination of the Σ underlying the ARPES spectra has remained a considerable challenge.

Here we present ARPES data obtained from optimally doped $Bi_2Sr_2CaCu_2O_{8+\delta}$, with excellent energy and momentum resolution, and employ a method of analysis allowing a detailed evaluation of the self energy along the $(0,0) \rightarrow (\pi,\pi)$ direction as a function of both binding energy and temperature. Overall, the imaginary component of Σ measured here is very different from that expected for a Fermi liquid or indeed that measured in normal metals (*6*). In the former, the width or scattering rate as determined by electron-electron interactions should have an ω^2 and T^2 dependence (where ω is the binding energy). In most metals, the electron-phonon interaction dominates. The self energy due to this interaction displays a rapid change in the scattering rate in the vicinity of the Fermi level and saturation at higher energies (*7*). However, in the present study of a high-temperature superconductor, we find possible evidence for quantum critical behavior. The possibility of such behavior has recently been discussed in several models of high-T_c superconductivity (*8*). In a quantum critical system, a phase transition can occur at zero temperature. As such, the transition is driven by quantum fluctuations rather than thermal fluctuations.

The present measurement can also be tied to conductivity measurements of the bulk material. Transport indicates that for optimally doped compounds, the resistivity in the normal state, and thus the inverse lifetime at the Fermi level, is linear with temperature over a wide range (*9*). Furthermore, infrared studies indicate that the scattering rate is linear in both temperature and frequency (*10*).

The photoemitted intensity in the $(0,0) \rightarrow (\pi, \pi)$ direction of the Brillouin zone (Fig. 1), as indicated by the arrow in the upper left inset, represents a 2D intensity map with binding energy in one dimension and momentum in the

[1]Department of Physics, [2]National Synchrotron Light Source, [3]Division of Materials Sciences, Brookhaven National Laboratory, Upton, NY 11973–5000, USA. [4]Department of Physics, University of Connecticut, Storrs, CT 06269, USA. [5]School of Physics, The University of New South Wales, Post Office Box 1, Kensington, New South Wales, Australia 2033. [6]Superconductivity Research Laboratory, ISTEC, 10-13, Shinonome I-chrome, Koto-ku, Tokyo 135, Japan.